Electro-aeromechanical modelling and feedback control of actuated membrane wings

Stefano Buoso* and Rafael Palacios†

Imperial College, London, SW7 2AZ, United Kingdom

This paper presents a numerical investigation on the potential for unsteady aerodynamic control on integrally-actuated membrane wings made of dielectric elastomers (DEs). They combine the advantages of membrane shape adaptability, which produces increased lift and delayed stall, with the benefits of simple, lightweight but high-authority control mechanism offered by integral actuation. High-fidelity numerical models have been developed to predict their performance and include a fluid solver based on the direct numerical integration of the unsteady Navier-Stokes equations, an electromechanical constitutive material model and a non-linear three-dimensional membrane structural model. Numerical results show that harmonic actuation of 5.0 kV gives an overall increase in the aerodynamic efficiency a fixed wing configuration the wing of up to 6.0%, measured as the lift-to-drag ratio. In addition, the definition of a reduced order model based on POD modes of the complete high-fidelity system allows the synthesis of a feedback control system to obtain on-demand aerodynamic performance.

Nomenclature

B_{ij}	Right Cauchy deformation tensor
$\mathbb{C}_{ijkl}$	Tangent stiffness matrix
C_{ij}	Left Cauchy deformation tensor
C_d	Drag coefficient
C_l	Lift coefficient
C_p	Pressure coefficient
E	Electric field magnitude, Young's modulus
F_{ij}	Deformation gradient
J	Determinant of the deformation gradient
J_m	Gent model material constant
K	Controller gain
P	Pressure
q	Dynamic pressure
S_{ij}	Second Piola-Kirchhoff stress tensor, snapshot matrix
U	Volumetric strain energy function
V	Velocity magnitude, voltage, volume
v_i	Velocity vector
W	Electromechanical strain energy function

Greek Letters

α	Angle of attack, summation index
ϵ	Dielectric permittivity
λ	Stretch
μ	Shear modulus
ν	Poisson ratio
ρ	Density
σ_{ij}	Stress tensor component
τ	Time constant, integration parameter
τ_{ij}	Shear stress component
$\Phi^{m\times k}$	Projection matrix
Φ	Deviatoric mechanical energy function
φ	Base function

Subscripts

e	Elastic
el	Electromechanical
m	Mechanical
s	Structural
V	Voltage
v	Viscous
∞	Equilibrium elastic, Free streem
0	Initial, Reference, Vacuum

Symbols and operators

$<\dot{\bullet}>$	Time derivative

*Graduate Student, Department of Aeronautics, 363A Roderic Hill Building; s.buoso12@imperial.ac.uk.

†Reader, Department of Aeronautics, 355 Roderic Hill Building; r.palacios@imperial.ac.uk. AIAA Member.

I. Introduction

Outdoor use of Micro Air Vehicles (MAVs) requires very high efficiencies to compensate for power limitations. In addition, their sensitivity to flow disturbances necessitates an enhancement of their stability and controllability. Nature offers possible solutions to address those limitations, such as the membrane wings of bats, which offer superior aerodynamic performance compared to rigid wings, such as delayed stall, higher lift, manoeuvrability and agility.[1–6] The skeleton stretching the membrane is an efficient control mechanism to tune in real time the aerodynamic characteristics of the wing. Similarly, MAVs embedded with fixed actuated membrane wings could provide on-demand aerodynamic performance. Dielectric elastomers (DEs) could combine the advantages of membrane wings with the benefits of a simple, lightweight control mechanism, and lead to the increase of specific performance necessary for the outdoor flight of MAVs.

The key characteristics of the physical system are highlighted in Fig.1. It is a heavily multidisciplinary problem, covering aerodynamics, structural dynamics, material modelling and control aspects. From the aerodynamic point of view Rojratsirikul *et al.*[3] have shown that, for Reynolds numbers typical of MAVs applications ($10^4 - 10^5$), separation and recirculation are the main source of unsteadiness in the interaction with the membrane, and cause the strong coupling between the fluid and the membrane vibrations.[3–5] Importantly, chordwise and spanwise modes were identified in low-aspect-ratio, $\mathcal{AR}$, rectangular membrane wings due to the coupling of tip vortices with the ones generated by the leading and trailing edge.[5,7] The coupling is influenced by the membrane prestrain and excess of length.[4] Arbos *et al.*[6] have experimentally shown that mean camber and modes of membrane aerofoils are strongly influenced by the size and shape of the leading- and trailing-edge supports.

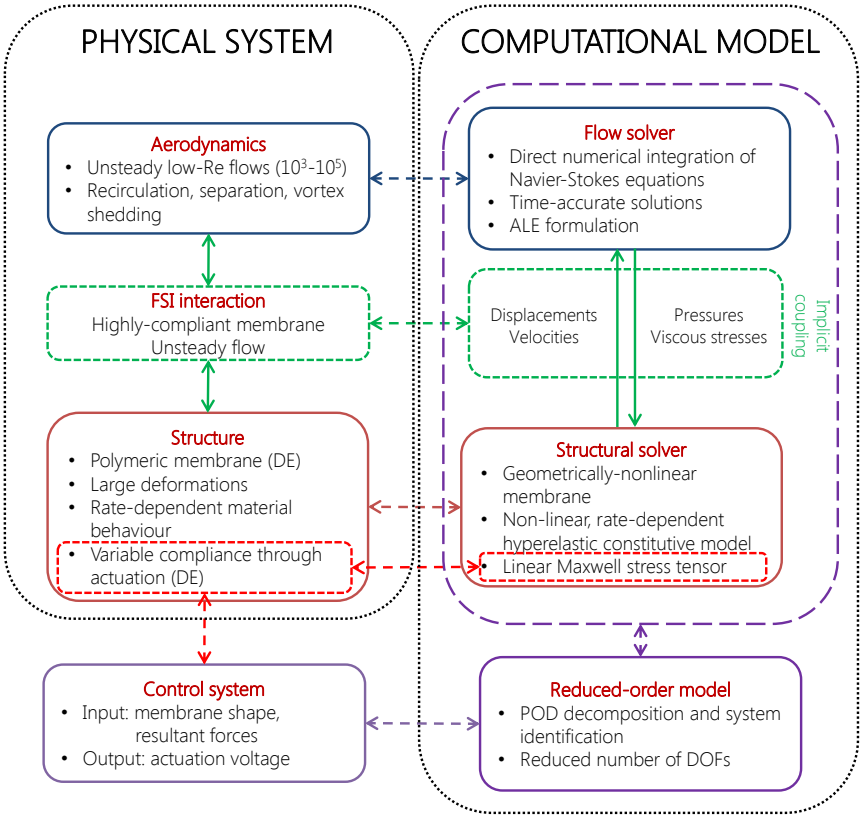


Figure 1: Definition of the aeroelastic problem of actuated membrane wings: physical system and the corresponding computational model used in this work.

On the structural side, the highly compliant system presents large deformations and a rate dependent constitutive behaviour because of the polymeric materials considered, and a variable compliance obtained through the electric actuation of the DE. Some experimental characterisation tests[8–10] on DEs are available in the literature. Fox and Goulbourne[8,9] have carried out a series of static and dynamic tests in circular

inflated DE membranes that are representative of the effective loading conditions for MAVs wings. They found that, when actuated with an harmonic voltage, viscoelastic effects can introduce significant delays in the dynamic response of the membrane and that viscoelastic stresses are not negligible.

To the authors' knowledge only Hays *et al.*[11] and Curet *et al.*[12] have to date experimentally tested the use of DEs to increase the performance of membrane wings. Hays *et al.*[11] investigated the gain in aerodynamic performance achievable with an integral static actuation, showing an increase in the lift-to-drag ratio for different angles of attack. Curet *et al.*[12] considered a dynamic actuation of the wing for different AoA. They identified optimum combinations of voltage amplitudes and frequencies to achieve the maximum aerodynamic efficiency of the wing.

From the computational point of view, in the literature there are no coupled high-fidelity models for actuated membrane wings that can consider all the fields involved and their interaction (see Fig. 1).

Earlier numerical models of passive flexible membrane wings were developed to study sail performance.[2] Smith and Shyy[13] compared the static deformed shapes of a 2D elastic membrane in potential and laminar flows confirming that viscosity plays an important role on the aerodynamic performance of the wing, in particular for high membrane cambers and angles of attack. The influence of membrane rigidity, pretension, angle of attack and Reynolds number for a 2D membrane in a laminar flow (Re= 2500-10000) has been investigated by Tiomkin *et al.*[14] and Gordnier.[15] Tiomkin *et al.*[14] have investigated static equilibrium configurations for the different parameters considered, together with dynamic results. Gordnier[15] investigated different flow conditions showing that vibrations due the coupling with the fluid increase with the angle of attack. Lian *et al.*[16] and Lian and Shyy[17] investigated the performance and the effect of spanwise vibrations of a low $\mathcal{AR}$ membrane wing considering an hyper-elastic material model. They coupled the MAV structural model with a e^N transition model for the fluid to capture the laminar-turbulent transition and the unsteady separation bubble. Lian *et al.*[16] obtained a good matching with experiments in the prediction of transition location, aerodynamic coefficients, and overall flow structures. However transitions models require a calibration of the parameters to the specific case, lacking the robustness required for general applications. Visbal[18] proposed an implicit large eddy simulation (LES) model where sub-grid models are discarded and the dissipative effect of the smaller-scale turbulence is obtained through numerical dissipation, which can be also artificially added to the system.

For the constitutive model, a comparison with experimental results indicates that a linear approach is not appropriate for DE with large strains and loading/unloading cycles.[10] Mokarram *et al.*[19] modelled the viscoelastic behaviour of DE using a multiplicative decomposition of the deformation gradient. The comparison of the results with tensile tests showed a good agreement for a wide range of deformation velocities, both for loading and unloading conditions. This model is however limited to unixial loading conditions. A dynamic model for the inflated circular membranes made of VHB4905 has been proposed by Buoso and Palacios.[20] The static part has proven to be predictive of the behaviour of inflated membranes used in different conditions.[21] The dynamic model is in good agreement with the experimental data and can capture the dynamic response of the membrane for the relatively low frequencies of interest in MAV applications.

All previous high-fidelity models are required for simulations, but a simplified description is needed for control design. Several model reduction techniques have been proposed in the literature for aeroelastic systems, including Volterra series,[22] proper orthogonal decomposition[23] (POD), balanced truncation and co-prime factorisation.[24] POD has also been widely used in the postprocessing of results for unsteady aerodynamics,[25] structural dynamics[26] and, in a more limited way, fluid-structure interaction problems.[27–29] Some efforts have already been done in the use of POD to analyse the flow field around a membrane wing.[30]

The reduced-order model description can be used in the system identification of the complete aeroelastic model of the membrane wing and the control system design. Linearity is often assumed[31] in this case but some works have proposed parameter dependent functions to take into account the variation of the system properties with its states.[27]

This work will investigate the potential gain in performance of dynamically actuated membrane wings in low Reynolds number flows. Section II presents a non-linear constitutive model for the DE, with a linear electrostatic model for the Maxwell stresses. This has shown to be a good approximation to the material behaviour in practical situations, but the model is capable of dealing with electrostrictive effects as well. The viscoelastic contribution of the constitutive model are not included in the simulations of this paper to reduce the complexity of the problem. In Section III the structural model is coupled using an implicit time marching algorithm with non-matching spatial discretisations, with a flow solver based on the direct

numerical integration of the unsteady Navier-Stokes equation. The dynamic aeroelastic model proposed has been compared with numerical results from the literature[14, 15] showing a good agreement both for the static and dynamic cases. In Section IV, POD is used for the model reduction and system identification of the full aeroelastic system. The resulting linear model is used to synthesise a simple control system for the wing that tracks a pre-defined aerodynamic performance.

II. Membrane Structural Models

Two structural models for membrane behaviour will be used in this work. The first model assumes ideal membrane behaviour: bending and transfer shear stiffness for the membrane structure are not included, neither the degree of freedom in the through-the-thickness direction. This simplified model is used to define reference solutions for validation and will use a discretisation based on four-nodes planar elements with translational degrees of freedom only.[32] The second model also allows stresses in the thickness direction, such that the electrostatic stress tensor can be defined in all three dimensions of the element. Commonly the effect of the Maxwell stress is modelled as an equivalent through-the-thickness compressive stress or an in-plane relaxation stress,[39] using the incompressibility assumption, but for high voltages this might not be true and require the definition of the real stress tensor. This model will be solved using solid elements and it is used in the dynamic coupling with the viscous flow solver. Elements are eight-nodes three-dimensional elements with translational degrees of freedom.[32] Both models coincide when the thickness of the membrane tends to zero, but the second model predicts a slightly stiffer structure because of the inclusion of the smaller, but not negligible bending and transfer shear stiffness. This second model is discussed next in some detail.

II.A. Visco-Hyperelastic Material Model for DEs

The viscoelastic constitutive model for DE considered in this work is developed in the finite deformation framework.[33–35] Let $\mathscr{B}_0$ be the reference configuration of a body at time t_0 and $\boldsymbol{\phi}$ the mapping function from $\mathscr{B}_0$ to the current configuration $\mathscr{B}$ at time t (Fig. 2). Let $\boldsymbol{F}$ be the *deformation gradient* of $\boldsymbol{\phi}$ expressed in the reference configuration and consider its multiplicative decomposition[36] into its volumetric and isochoric components, that is,

$$\bar{\boldsymbol{F}} = \boldsymbol{F} J^{-\frac{1}{3}}, \tag{1}$$

where $\bar{\boldsymbol{F}}$ maps the isochoric deformation of the body and $J = \det(\boldsymbol{F})$ is related to the change in volume. $\bar{\boldsymbol{F}}$ and J are used to define the elastic deviatoric and hydrostatic stresses in the deformed configuration.

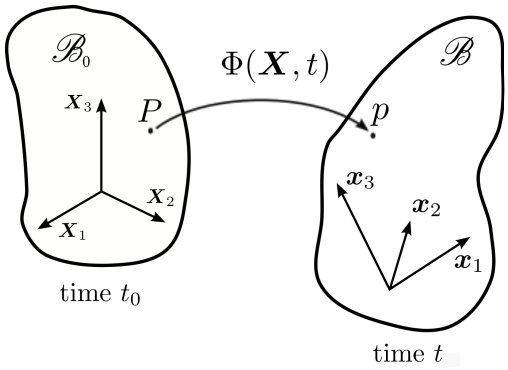


Figure 2: Reference and actual configurations.

The viscous contribution, that is assumed to be purely deviatoric, is expressed in terms of a number of elastic tensors, $\bar{\boldsymbol{F}}_{e\alpha}$, with $\alpha = 1, ..., N$, related to $\bar{\boldsymbol{F}}$ by[33]

$$\bar{\boldsymbol{F}}_{e\alpha} = \bar{\boldsymbol{F}} \boldsymbol{F}_{v\alpha}^{-1}, \tag{2}$$

where $\boldsymbol{F}_{v\alpha}$ is the viscous tensor associated to the α-th viscous mechanism. $\boldsymbol{F}_{v\alpha}$ represents the internal variables describing the nonequilibrium evolution of the material constitutive law

$$\dot{\boldsymbol{C}}_{v\alpha} = \frac{1}{\tau_\alpha} \left[\boldsymbol{C} - \boldsymbol{C}_{v\alpha} \right] \tag{3}$$

where $\boldsymbol{C}$ is the right Cauchy deformation tensor and, given the deformation gradient $\boldsymbol{F}$, it is defined as

$$\boldsymbol{C} = \boldsymbol{F}^T \boldsymbol{F} \tag{4}$$

and τ_α is the time constant relative to the α relaxation mechanism. Similar expressions define the elastic and viscoelastic tensors. Eq. (3) is a linearisation of the one proposed by Bonet.[34] For details on the general derivation of the evolution law, the reader is referred to the work of Bonet.[33,34] The evolution of the internal variables from the initial condition considered, is driven by the loading conditions represented by $\bar{\boldsymbol{F}}$. The thermodynamic equilibrium is reached when $\boldsymbol{C}_{v\alpha} = \bar{\boldsymbol{C}}$. Thus at equilibrium $\bar{\boldsymbol{F}}_{e\alpha} = \boldsymbol{I}$ and hence the viscous stresses are zero.

In this work, an isotropic constitutive model is assumed. This has been experimentally verified on DEs up to a stretch of around 1.5,[37] but would need further investigation for higher stretches. The mechanical free-energy function of an isotropic material can be expressed in terms of the invariants of the right Cauchy-Green deformation tensors. For the elastic component $\bar{\boldsymbol{C}} = \bar{\boldsymbol{F}}^T \bar{\boldsymbol{F}}$ and for the viscoelastic one $\bar{\boldsymbol{C}}_{e\alpha} = \bar{\boldsymbol{F}}_{e\alpha}^T \bar{\boldsymbol{F}}_{e\alpha}$.[34] Given a generic tensor $\boldsymbol{C}$ the invariants considered are

$$I_1 = \mathrm{tr}\boldsymbol{C} \qquad I_2 = \frac{1}{2}\left((\mathrm{tr}\boldsymbol{C})^2 - \mathrm{tr}\boldsymbol{C}^2\right) \tag{5}$$

Thus the free energy function is of the form

$$W = U(J) + \Phi_\infty\left(\bar{I}_1, \bar{I}_2\right) + \sum_{\alpha=1}^{N} \Phi_{v\alpha}\left(\bar{I}_{1_{e\alpha}}, \bar{I}_{2_{e\alpha}}\right) \tag{6}$$

where $U(J)$ is the volumetric energy function accounting for the variation in volume defined by J, $\Phi_\infty\left(\bar{I}_1, \bar{I}_2\right)$ is the deviatoric free energy function and $\Phi_{v\alpha}\left(\bar{I}_{1_{e\alpha}}, \bar{I}_{2_{e\alpha}}\right)$ is the energy function corresponding to the viscoelastic stresses related to the α-th mechanism. $\bar{I}_{1_{e\alpha}}$ and $\bar{I}_{2_{e\alpha}}$ are the first and second invariants of $\bar{\boldsymbol{C}}_{e\alpha}$.

In this work, the elastic constitutive law for DE will the Gent incompressible model[38]

$$\Phi_\infty = -\frac{\mu J_m}{2}\log\left(1 - \frac{I_1 - 3}{J_m}\right) \tag{7}$$

where μ and J_m are determined from experiments. This model is used because it consists of two parameters of immediate physical significance and it predicts the stiffening behaviour when the deformation approaches the value of the limiting stretch.

The stresses are the coniugates with respecto to the free energy function of the stretches in the directions considered.[34] The second Piola-Kirchhoff stress tensor $\boldsymbol{S}$ represents the stresses expressed in the reference configuration and is obtained as

$$\boldsymbol{S} = 2\frac{\partial W}{\partial \boldsymbol{C}} = \boldsymbol{S}_J + \boldsymbol{S}_\infty + \boldsymbol{S}_v = J\frac{\partial U}{\partial J}\boldsymbol{C}^{-1} + 2J^{-\frac{2}{3}}\mathbb{P} : \left(\frac{\partial \Phi_\infty}{\partial \bar{\boldsymbol{C}}} + \frac{\partial \Phi_v}{\partial \bar{\boldsymbol{C}}}\right) \tag{8}$$

where $\boldsymbol{S}_J$ are the stresses due to the contribution of the volumetric energy function, $\boldsymbol{S}_\infty$ is the contribution of the elastic deviatoric stresses, $\boldsymbol{S}_v$ the viscous stresses, and the projection tensor is $\mathbb{P} = \mathbb{I} - \frac{1}{3}\boldsymbol{C}^{-1} \otimes \boldsymbol{C}$ with $\mathbb{I}$ the fourth-order identity tensor. The mechanical stress tensor in the deformed configuration $\boldsymbol{\sigma}_m$ is finally obtained through a push-forward operation on $\boldsymbol{S}$

$$\boldsymbol{\sigma}_m = \frac{1}{J}\boldsymbol{F}^T \boldsymbol{S} \boldsymbol{F} \tag{9}$$

The constitutive model is completed by adding the effect of the electrostatic stresses that are modelled with the Maxwell's stress tensor. Given an electric field vector $\boldsymbol{E}$, the stress tensor $\boldsymbol{\sigma}_e$ is defined as[39]

$$\boldsymbol{\sigma}_e = \epsilon \boldsymbol{E} \otimes \boldsymbol{E} - \frac{1}{2}\epsilon\left(\boldsymbol{E} \cdot \boldsymbol{E}\right)\boldsymbol{I} \tag{10}$$

where ϵ is the material dielectric constant, $\boldsymbol{E}$ is the electric field vector in the deformed coordinate system and $\boldsymbol{I}$ is the unitary second order tensor. The material dielectric constant ϵ is usually expressed as $\epsilon = \epsilon_0 \epsilon_r$

where ϵ_0 is the vacuum dielectric constant and ϵ_r is the material relative dielectric constant. The total stress is finally obtained as $\boldsymbol{\sigma}$[39]

$$\boldsymbol{\sigma} = \boldsymbol{\sigma}_m + \boldsymbol{\sigma}_e \tag{11}$$

These constitutive equations proposed have been implemented in the Finite Element (FE) package ABAQUS. An implicit iterative scheme is used to obtain the stresses in terms of $\boldsymbol{C}$ and $\boldsymbol{C}_e$ at the end of each time increment. The evolution law (3) for the internal variables is integrated with an implicit Euler scheme. The tangent stiffness matrices are recomputed at every iteration considering the actual geometry and stresses in the material. The equilibrium system is solved using an iterative Newton-Raphson scheme. The tangent stiffness matrix $\mathbb{C}$ in the reference configuration is obtained as[34,40]

$$\mathbb{C} = 2\frac{\partial \boldsymbol{S}}{\partial \boldsymbol{C}}, \tag{12}$$

with $\boldsymbol{S}$ defined as (8). The tensor is finally written in the deformed coordinate system by means of a push forward operation $\mathbb{C}^a_{ijkl} = F_{ip}F_{jq}F_{kr}F_{ls}\mathbb{C}_{pqrs}$.

III. Aeroelastic Model

As with the structural analysis, two different model fidelities for the fluid solver are considered in this work. A static Vortex Lattice Model (VLM) is first implemented to compute an inviscid flow around the membrane and it is used in the validation of the coupling of the structural and fluid solver and for a first estimation of membrane static equilibrium. To account for the effects of viscosity and dynamics, a viscous flow solver is considered to describe the low-Reynolds flow around the membrane.

III.A. Inviscid flow solver

The first model is the static Vortex Lattice Model and assumes irrotational, inviscid attached flow. This simplification allows a first estimation of the pressure loads on the wing with a low computational cost.[41,42] The model is based on the discretisation of the wing surface and wake with vortex rings. A control point is defined in the centre of each vortex ring, which is composed by four straight segments with constant vortex intensity, Γ. The effect of each segment on a control points can be obtained integrating the Biot-Savart law along each segment length.

The global effect of each vortex ring on each of the control points is obtained summing the contributions of its four segments. Assuming unitary vortex intensity, its normal component to the panel becomes a purely geometric parameter depending only on the wing and wake geometries. It is also known as the influence coefficient of the between the two panels considered. All the coefficients forms the entries of the matrix of the influence coefficients $\boldsymbol{A}$, which defines the aerodynamic linear system whose unknowns are the vortex intensities of each panel which are unequivocally defined with the flow boundary conditions of the problem.

$$\boldsymbol{A}\{\boldsymbol{\Gamma}\} - \{\boldsymbol{V}_{\infty,n}\} = 0 \tag{13}$$

where $\boldsymbol{V}_{\infty,n}$ represents the flow boundary conditions of the problems, obtained considering the projection of the free stream velocity on the normal to each panel. From the vortex intensities the pressure on distribution on the wing can be computed. In a non-linear static aeroelastic problem, the deformation of the structure with the pressure loads requires a recalculation of $\boldsymbol{A}$ to account for the new wing geometry.

III.B. Viscous flow solver

The second fluid model considered is a viscous flow solver for relatively low Reynolds number flows. It is based on the finite-volume discretisation of the Navier-Stokes equations implemented in STAR-CCM+.[43] The low Mach number of the wing applications allow for the incompressibility assumption, but the solver is based on the compressible equations to reduce instability issues.[43] A coupled approach is used to solve the flow and energy equations, which requires more memory but offers better stability and velocity in the convergence. Second-order accurate integration in space and time are used. The maximum number of sub-iteration for each time-step is set to 10 and the limit relative tolerance for the monitored flow properties is set to 10^{-4}. The boundary conditions defined includes a constant pressure boundary condition at the outlet, and the specification of velocity magnitude and direction for all other boundaries. In case a 2D case is considered,

periodic boundary conditions are imposed in the lateral surfaces of the domain. On the membrane walls a no-slip constrain is imposed. For each case considered, a mesh-refinement and time-step sensitivity study has been conducted. For the dynamic cases considered, the relative errors on the mean value of C_l and C_d as well as the amplitudes and frequencies of the oscillations of their values were considered to establish convergence. The maximum relative error of those quantities was set to be below 2%. In addition to the sensitivity to the grid-resolution and time step, for each case considered the element size and time step have been compared with the characteristic viscous length and time scales, respectively[44]

$$l_\nu = \frac{\nu}{u_\nu} \tag{14a}$$

$$t_\nu = \frac{l_\nu}{u_\nu} = \frac{\nu}{u_\nu^2} \tag{14b}$$

where ν is the kinematic viscosity of the fluid and u_ν is the friction velocity defined as[44]

$$u_\nu = \sqrt{\nu}\,(S_{ij}S_{ij})^{\frac{1}{4}} \tag{15}$$

with S_{ij} being the symmetric part of the velocity gradient, $S_{ij} = \frac{1}{2}\left(\frac{\partial V_i}{\partial x_j} + \frac{\partial V_j}{\partial x_i}\right)$, and V the flow velocity. Assuming a volumetric average of the elements size, the characteristic length of the mesh elements is $l_{mesh} = \sqrt[3]{l_x l_y l_z}$ with l_x, l_y and l_z being the dimensions of the hexahedral cells. The correct spatial and temporal resolution of the smallest turbulence scales requires to have[44,45]

$$l^* = \frac{l_{mesh}}{l_\nu} \sim \mathcal{O}(1) \tag{16a}$$

$$t^* = \frac{\Delta t}{t_\nu} \sim \mathcal{O}(1) \tag{16b}$$

where Δt is the time step of the implicit solvers. The fluid mesh selected for the simulations are well within this range, with a value of l^* and t^* below 3 throughout the domain.

III.C. Fluid-Structure Coupling

The coupling with the inviscid flow solver is obtained by embedding the (quasi-steady) VLM solver in the FE solver. The Vortex Lattice Method receives as inputs the nodal displacements of the structure and uses those variables for the calculation of the geometric variables for the definition of the matrix $\boldsymbol{A}$ and the vector $\boldsymbol{V}_{\infty,n}$ of Eq. (13). The linear aerodynamic system is solved in an internal loop at each iteration of the FE solution. For each element the calculated pressure distribution obtained is discretised in nodal forces using the shape functions of the elements considered. The new nodal displacements are then calculated by the FE solver and the process is iterated till static equilibrium is found. If the wing is modelled with solid elements (Section II), the nodes of the suction surface are considered as reference for the vortex ring distribution.

The coupling of viscous flow solver and structural one requires both parts to occupy the same spacial positions in the models, allowing the mapping of the nodes of the elements of the two meshed considered. Once neighbour nodes and elements are identified, the fluid solver uses the shape functions of the structural solver for the interpolation of the pressure and viscous forces and the definition of the equivalent set of nodal loads to be used in the Finite Element solver.[43] The new nodal displacements and velocities from the FE solver are then passed to the fluid solver for the deformation of the mesh and the computation of the new flow field. The mesh deformation process moves the mesh nodes accordingly to a 3D linear interpolation law that is depending on their distance from the moving and fixed boundaries. An implicit coupling was found necessary, considering the strong interaction of the fluid and the membrane structure in this problem. When the relative difference in the norm of two consecutive field exchanges is below a defined tolerance, 10^{-4} for the results in this work, convergence is established. The exchange of data between the solvers uses a bridge in the RAM memory.[43]

IV. System Identification

POD, also known also as discrete Karhunen-Love[46,47] decomposition, is used here to reduce the size of the aeroelastic system[48,49] and facilitate control design. The basic idea behind POD is the approximation

of a function $\mathbf{G}(\mathbf{x},t)$ with a combination of basis functions $\boldsymbol{\varphi}_i(\mathbf{x})$ such as

$$\mathbf{G}(\mathbf{x},t) \approx \sum_{i=1}^{m} a_i(t)\boldsymbol{\varphi}_i(\mathbf{x}), \tag{17}$$

where $a_i(t)$ are time dependent weights. They are determined with a minimisation process in the least square sense

$$\min \parallel \mathbf{G}(\mathbf{x},t) - \sum_{i=1}^{M} a_i(t)\boldsymbol{\varphi}_i(\mathbf{x}) \parallel_{\mathcal{L}^2} \tag{18}$$

where $\parallel \bullet \parallel_{\mathcal{L}^2}$ indicates the $\mathcal{L}^2$-norm and the coefficients $a_i(t)$ are given by

$$a_i(t) = \int \mathbf{G}(\mathbf{x},t)\boldsymbol{\varphi}_i(\mathbf{x})dx. \tag{19}$$

When dealing with a function sampled in m discrete points and n time steps, as can be the time history of variables of a simulation or data from experimental results, the calculation of the basis functions is done here through the so called *snapshot method*. It consists in the definition of a snapshot matrix $\mathbf{S}$

$$\mathbf{S} = \Big[\mathbf{u}(\mathbf{x},t_1), \quad \mathbf{u}(\mathbf{x},t_2), \quad . \quad . \quad . \quad , \mathbf{u}(\mathbf{x},t_n)\Big], \tag{20}$$

which is a $m \times n$ matrix whose columns $\mathbf{u}(\mathbf{x},t_i)$ are the vectors of the values of function $\mathbf{G}(\mathbf{x},t)$ at m discrete points considered and at time $t = t_i$. It has been proven[46,47] that in this case the basis functions that minimise (18) are obtained projecting $\mathbf{S}$ on the eigenvectors $\mathbf{V}_i$ of the correlation matrix $\mathbf{S}^T\mathbf{S}$. We define then

$$\boldsymbol{\Phi}_{global} = \mathbf{S}\mathbf{V}\boldsymbol{\lambda}^{0.5}, \tag{21}$$

where $\boldsymbol{\Phi}_{global}$ is a $m \times n$ projection matrix, whose columns are the basis functions of the POD decomposition

$$\boldsymbol{\Phi}_{global} = \Big[\boldsymbol{\varphi}_1(\mathbf{x}), \quad \boldsymbol{\varphi}_2(\mathbf{x}), \quad . \quad . \quad . \quad , \boldsymbol{\varphi}_n(\mathbf{x})\Big], \tag{22}$$

$\mathbf{V}$ is the matrix whose columns are the eigenvectors $\mathbf{V}_i$ of the correlation matrix, and $\boldsymbol{\lambda}$ is a diagonal matrix containing the eigenvalues of $\mathbf{S}^T\mathbf{S}$. In general, the number of basis function chosen, k, for the definition of the projection matrix $\boldsymbol{\Phi}$ used in the POD decomposition, is much smaller than n and depends on the level of accuracy of the description that is required.

The discrete form of (19), for the calculation of the time dependent coefficients $a_i(t)$ for each of the k POD modes considered, consists in the projection of $\mathbf{S}$ onto the projection matrix $\boldsymbol{\Phi}$ built with the k basis considered

$$\mathbf{a}(t) = \begin{bmatrix} a_1(t) \\ a_2(t) \\ . \\ . \\ . \\ a_k(t) \end{bmatrix} = \boldsymbol{\Phi}^T\mathbf{S}, \tag{23}$$

where the i-th row of the matrix $\mathbf{a}(t)$ contains the time history of the amplitude of $a_i(t)$. The amplitudes of the basis function are the new variables of the system. In this way the number of variables is reduced from m to k, where $k \ll m$. This model reduction is very appealing in the context of system identification, because it significantly reduces the number of variables that have to be determined, but it may have very slow convergence and local validity.

V. Numerical Results

The first set of results is from a static coupling of the inviscid flow solver (Section III) with the structural models of Section II. It will be used to assess issues related to the static aeroelasticity of membrane wings and provide some insight on how the membrane deforms for different angles of attack, flow velocities and

membrane section rigidity. Then, using a the viscous fluid model, it is investigated the static and dynamic behaviour of the 2D elastic membrane. The numerical results from the models proposed will be compared with those obtained by Tiomkin et al.[14] and Gordnier.[15] After the verification of the model, the constitutive model of the DE proposed in Section II.A (which was already exercised in[20]) will be used to investigate the effects of the integral actuation on wing aerodynamic performance. In the final part, the numerical results proposed will be used to define a ROM through proper orthogonal decomposition and define a PID control system for the membrane. The resulting control mechanism will be implemented in the high-fidelity model and compard with the prediction of the reduced order model considered.

V.A. Verification against analytical model for low AoA

A static aeroelastic model of an inextensible 2D membrane at low AoA in an inviscid and irrotational flow is first discussed. The model is based on the assumption that the membrane deformed shape in the 2D case can be approximated with a symmetric parabola. This is supported by the experimental work of Song *et al.*[50] and Molki and Breuer.[51]

Under these assumptions, the C_l of the 2D inextensible membrane is given by

$$C_l = 2\pi \frac{1}{1 - \frac{\pi}{4\Pi_\infty}} \alpha \tag{24}$$

where Π_∞ is $\frac{T_x}{\frac{1}{2}\rho V_\infty^2}$. Details in the derivation can be found in the Appendix. Eq. (24) states that, at small angles, there is still a linear relation between the lift coefficient and the angle of attack as for the rigid profile. The coefficient of linearity in this case includes the camber effect due to the deformation of the membrane. The higher the value of Π is, the lower the deformation of the membrane and hence the camber effects. The C_l tends to the flat plate solution for an infinitely rigid membrane (when T tends to an infinite value).

This analytical solution can be now compared to the numerical results from the aeroelastic model defined as in Section II. The membrane is a 3D Finite-Element model rigidly supported at leading- and trailing edges, with a chord length of 0.15 m and $\mathcal{AR}$ =100 in order to reduce the influence of tip effects at the mid-span position. The thickness is 50 μm, the linear prestrain is 0.4, the elastic modulus E= 10 MPa and zero Poisson's ratio is selected, in order to decouple the effect of the principal stresses and obtain a 2D solution. The free stream velocity is $V_\infty = 10$ ms^{-1} and the AoA considered are $\alpha = 2^\circ$ and 5°. Results are in Table 1. The case can be representative of a inextensible prestretched latex membrane wing. The deformed shape and the C_l are computed in the section in the centre of the span. A three dimensional vortex lattice method has also been coupled as described in Section III. Both elements provide a very good agreement with the analytical model. As underlined in Section II, the solid elements are slightly stiffer than membrane elements, and this explains the lower value of the lift coefficient, due to a reduced camber effect.

Table 1: Aeroelastic coupling of the passive membrane with potential-flow solver

Lift Coefficient Results		
Model	2°	5°
Analytical	0.2260	0.5650
Membrane Elements	0.2254	0.5628
Solid Elements	0.2205	0.5495

V.B. Viscous Flow Results

Initially the 3D membrane will modelled with no supports, as in Tiomkin *et al.*[14] A zero-displacement condition is imposed to the leading- and trailing-edges of the membrane, that is modelled with solid elements. The geometrically non-linear structural model allows for thickness variations and chord-wise and span-wise nodal displacements. The rectangular fluid domain boundaries are placed 50 chords far from the membrane in each direction and a structured mesh is used for the discretisation. A 2D case is now addressed to remove tip-effects and compare the results with those from Tiomkin *et al.*[14] Periodic boundary conditions are applied to the free edges of the membrane in both the structural and the fluid model to remove tips

effects. The membrane is solved in the structural model using 200 solid elements in the chord direction and one in the through-the-thickness direction. The fluid domain is solved using 400 elements along the membrane chord and 100 elements in the radial directions. The deformed shape and pressure distribution across the membrane is shown in Fig. 3 and corresponds to the static case of a 2D membrane for Re = 2500 and tension coefficient $C_T = \frac{T}{q_\infty c}$ equal to 2, where q_∞ is the free stream dynamic pressure. The AoA considered are $\alpha = 3°$ and 7°. The results are compared with the one from Tiomkin *et al.*[14] They proposed a numerical investigation of an aeroelastic model of a 2D membrane in a viscous flow. The model assumes a constant membrane thickness and a purely 2D membrane behaviour. The only degree of freedom in the 2D model is the vertical displacement of the points of the membrane. The numerical results obtained are in very good agreement, with differences of less than 1% for the displacement and 4% for the ΔC_p across the membrane. The small discrepancy in the results can be attributed to the differences between the structural models used: the model proposed in this work considers the changes in membrane thickness in both the fluid and structural models and allows for in-plane displacements, which results in some differences as the deformation increases. In addition, the higher stiffness of the solid elements when compared to membrane ones, determines a higher ΔC_p distribution when the same level of deformation is considered.

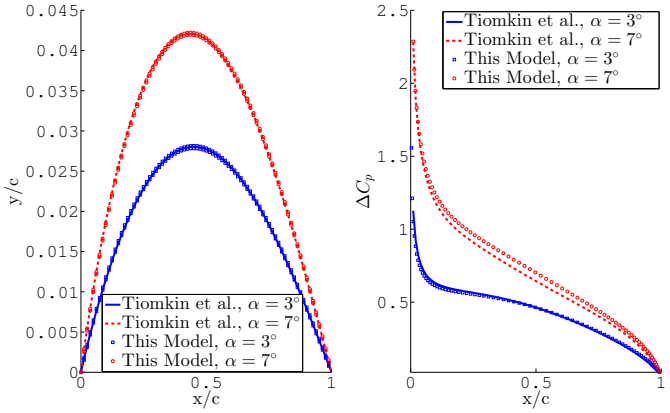


Figure 3: Displacements and pressure distribution on membrane with point rigid supports, $C_T = 2$

The second test case will study the accuracy of the current approach to capture the unsteady aerodynamics due to the effect of rigid supports. The support geometry is from the experimental setup by Rojratsirikul.[3] The chord is $c = 0.1366$ m, the thickness is $h = 0.2$ mm, and the membrane is mounted on the supports with zero prestrain $\delta_0 = 0$. The material is modelled with a linear elastic constitutive law with Young's modulus $E = 3346$ Pa, Poisson ratio $\nu = 0$ and density $\rho_s = 473$ kgm^{-3}. The flow has a free stream velocity $V_\infty = 0.2886$ ms^{-1}, density $\rho_f = 1.1767$ kgm^{-3} and dynamic viscosity $\mu_f = 1.855\text{e}^{-5}$ Pas. The angles of attack are considered, $\alpha = 4°$ and 8°. The non-dimensional parameters describing the 2D aeroelastic problem investigated, obtained by normalisation with c, V_∞, ρ_f, are $\overline{Eh} = 50$, $\delta_0 = 0$ and $\overline{\rho_s h} = 0.589$. In the structural model the supports are modelled as fixed rigid bodies and the membrane is solved using 200 solid elements in the chord direction. The fluid domain stretches 100 chords in the radial directions around the wing. The size of the domain has been determined after a sensitivity study of the dynamic response of the wing subjected to the different flow conditions considered. The mesh uses 200 elements around the supports, 200 on the membrane and 300 elements in the normal directions to the wing. From the results shown in Fig. 5 it is evident the effect of fixed supports on the aerodynamic performance of the wing. In particular the C_p distribution for $\alpha = 4°$ shows an earlier separation bubble starting from the leading edge and reattaching at about 10% of membrane chord. The present results are compared with the 2D calculations obtained by Gordnier,[15] who assumed a membrane structural model with constant and uniform thickness and only out-of-plane displacements. The flow field is solved using a sixth-order Navier-Stokes solver, allowing for a coarser mesh than the one used in this work. Fig. 5 shows a very good agreement of the mean deformed shapes and mean C_p distributions on the membrane for both cases considered. Numerical results showed convergence towards the same values proposed by Gordnier[15] and the small differences can be attributed to the differences in the structural models considered and to the simplification of the supports of the geometry used in the model proposed. In fact, from Fig. 5 the main differences in the results are in proximity of the

end of the leading-edge support (x=0 in the plot), which, in our case, was modelled without the sudden step at its end. Increasing the incidence angle, the effect of wake instabilities increases in importance causing the membrane to oscillate over the mean configuration with increasing amplitudes. When the angle of attack is 8°, the system exhibits a self excited oscillatory behaviour, with a dominant third membrane mode with a frequency of St=1.45, as reported by Gordnier.[15] This comparison demonstrated the suitability of the current solution method to represent the dynamics of the membrane wings at moderate angles of attack.

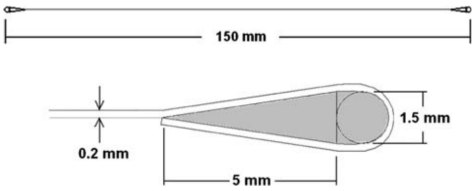


Figure 4: Wing geometry and detail of support.[3]

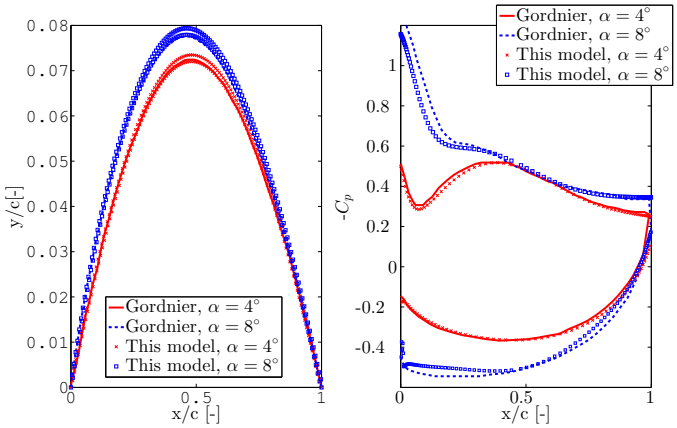
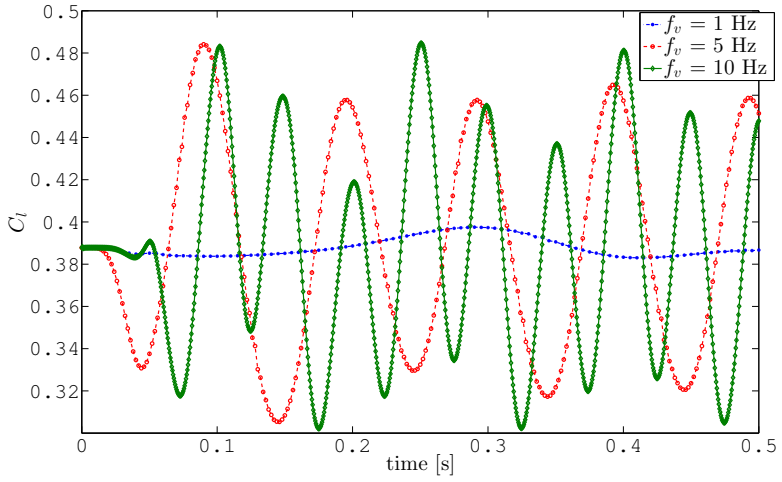


Figure 5: Displacements and pressure distribution on membrane with solid rigid support. Gordnier's displacement results refer to the mean value (continuous and dotted lines in the plot). In this work the membrane thickness is modelled in both solvers, generating two series of results referring to the suction and pressure surfaces.

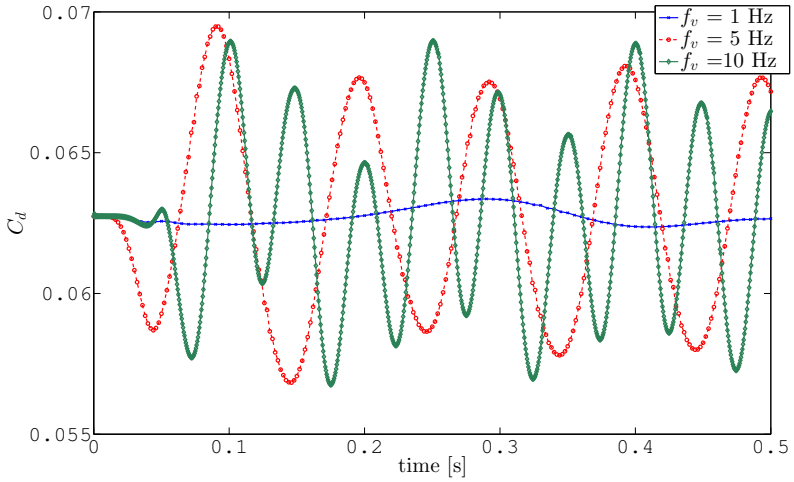
V.C. Actuation of the membrane

The electromecanical material model proposed in Sec.II.A, which was compared against experimental data,[20] is here coupled with the aeroelastic model from Sec.III to investigate the performance of an integrally actuated 2D membrane wing made with of VHB4905 elastomer. The viscoelastic part of the constitutive model is not included to limit the complexity in the analysis. The resulting material model is then less stiff and does not introduce time delays due to viscoelastic effects. The coefficients of the Gent material model used are μ= 20 kPa and J_m= 100[20] and the relative dielectric constant is $\epsilon_r = 2.7$ to match the experimental of Refs.[8,9] The same flow conditions and geometric parameters of Sec.V are used. The membrane prestretch is set to 2, to reduce the voltage required for the actuation of the wing. The initially steady, passive case with α = 4° is considered. The time step used is of the order of 10^{-4} s and showed enough temporal resolution of the relevant time-scales of the problem. The mesh-size and refinement are case dependent and varied from around 250k elements to 1 million elements when the domain size is set to 100 times the chord length and Re = 2500. In all cases, the smaller elements around the membrane walls have a thickness of 50μm as well as the through-thickness elements, and the bigger elements, at the domain boundaries, are the twice the size of the membrane chord. The voltage amplitude of the integral actuation on the membrane is 4.5 kV (as in Curet *et al.*[12]) with varying frequencies 1, 5 and 10 Hz. The effect of the actuation on the lift coefficient are presented in Fig.6. Results shows that the mean value of C_l, shown in Fig. 6a, is independent of the frequency of actuation and tends to a steady value that is determined by the amplitude of the voltage applied. On the

other side, the amplitude of the oscillations of the C_l depends on the frequency of the excitation and is higher with the higher membrane oscillations when the frequency of the Maxwell stresses applied is close to the natural frequency of the system, that is found to be close to 4 Hz. The same observations apply to the C_d, Fig. 6b. The results show that the actuation determines a reduction of the membrane pretension and a small increase in the camber amplitude. This determines an increase in the lift and drag coefficients. The global effect of the actuation on the aerodynamic performance can be measured considering the aerodynamic efficiency defined as C_l/C_d. Since the amplitude of the oscillations of C_l and C_d depends on the frequency, the instantaneous value of the efficiency is frequency dependent, but the mean value tends to a value that just depends on the amplitude of the applied voltage. In this case, with a voltage of 4.5 kV, an increase of 0.1% of is achieved for the steady state mean value.



(a) C_l



(b) C_d

Figure 6: Actuation of the membrane wing for $c = 0.15$ m, $\alpha = 4$ ° and Re = 2500. The voltage amplitude is 4.5 kV.

The poor increase in performance is mainly due to the high membrane stiffness of the case considered. The low camber and small structural oscillations obtained with actuation are not enough to determines an overall variation of the aerodynamic efficiency. To prove this, a different case is considered, with chord c = 0.03 m, prestretch = 1.02, Re = 2500 and $\alpha = 4°$. In this case the membrane is much more compliant. The reduction of c with the same Re number determines an increase in the inlet velocity which requires a

finer mesh to resolve the flow and a million elements are used. Again, in the passive case, the equilibrium configuration presents a steady camber with maximum amplitude of 2%. The membrane is then actuated with a uniform voltage V = 5 kV and frequencies 5 and 10 Hz. The variation of the mean lift and drag coefficients are reported in Table 2. The 5 Hz actuation case presents a net enhancement in the aerodynamic performance, due to the much higher increase in the mean lift as compared to the drag. On the other hand, the actuation with 10 Hz determines a clear reduction in the performance of the wing, due to the high increase of drag.

Table 2: Mean aerodynamic coefficients for the actuated membrane. Case with Re = 2500, $\alpha = 4°$, c=0.03 m, $V = 5$ Kv

$f_v[Hz]$	$\Delta C_l[\%]$	$\Delta C_d[\%]$	$\Delta efficiency[\%]$
5	+ 24.1	+ 17.0	+ 6.0
10	+ 7.7	+ 15.1	- 8.0

V.D. System identification

A reduced-order model for the 0.15 m long wing response presented in Sec.V.C is now obtained. This case is considered for simplicity, since the lower membrane displacements allow an easier handling of the problem. The passive membrane equilibrium configuration is considered as reference and a uniform pressure of magnitude $\Delta P = 0.1$ Pa is applied to the membrane, to obtain an increase of the mean camber within the linear structural regime. The frequency of the excitation is varied linearly with time in the range of [0.1 - 10] Hz from 0 to 2 s. The time step considered is 5×10^{-5} s. The displacement history of the points in the suction surface of the membrane is stored and the vertical position of the points defines the system variables. The chord-wise displacement of the points is 5 orders of magnitude smaller than the vertical displacements, so the chord-wise positions of the points are assumed to be constant. The vertical coordinates of all the points of the membrane at every time step are used to build the snapshot matrix as described in Section IV. The basis functions are computed initially with only 2 modes, giving a good compromise between accuracy of the approximation and cost of the parameters identification for the linear system. The displacements, velocities and accelerations histories of the points are projected onto the basis functions and respectively $\mathbf{a}_P(t)$, $\dot{\mathbf{a}}_P(t)$ and $\ddot{\mathbf{a}}_P(t)$ are obtained. The projection of the pressure history is $\mathbf{\Delta P}^* = \mathbf{\Phi}^T \mathbf{\Delta P}$.

The aeroelastic system is then modelled as a second order linear system

$$\mathbf{M}^* \ddot{\mathbf{a}}_P(t) + \mathbf{C}^* \dot{\mathbf{a}}_P(t) + \mathbf{K}^* \mathbf{a}_P(t) = \mathbf{\Delta P}^* \tag{25}$$

The coefficients of the mass, damping and stiffness matrices, $\mathbf{M}^*$, $\mathbf{C}^*$ and $\mathbf{K}^*$, are obtained imposing that (25) is satisfied at every time step in a least-square sense. Fig. 7 shows a comparison of the high-fidelity simulation of a point of the membrane, the POD reconstruction and the integration of the linear system obtained through the system identification. A very good agreement can be observed.

The electroactive part of the model, responsible of the membrane actuation, is identified actuating the membrane with a uniform voltage $V = 4.5$ kV. The frequency is varied linearly from 0.01 to 5 Hz in a time window of 2 s with a time step of $5{\times}10^{-4}$ s. The upper frequency boundary range is chosen to limit the resulting excitation frequency of the voltage to the maximum value considered in the mechanical system identification. The lower one allows the characterisation of the aeroelastic system at its first resonance peak.

The mechanical matrices of the reduced order model obtained for this case defined a dynamic system with the same dynamic properties of the previous one. Therefore, to obtain a linear system that can deal with both pressure variations and actuation in the same description, the same projection matrix and mass, damping and stiffness matrices as in the pressure case are here used. Displacements, velocities and accelerations histories of the points of the membrane with actuation are then projected, obtaining $\mathbf{a}_V(t)$, $\dot{\mathbf{a}}_V(t)$ and $\ddot{\mathbf{a}}_V(t)$. So the system is built as

$$\mathbf{M}^* \ddot{\mathbf{a}}_V(t) + \mathbf{C}^* \dot{\mathbf{a}}_V(t) + \mathbf{K}^* \mathbf{a}_V(t) = \mathbf{G}^* V^2, \tag{26}$$

where $\mathbf{G}^*$ is the gain matrix of the voltage signal. $\mathbf{M}^*$, $\mathbf{C}^*$ and $\mathbf{K}^*$ are the matrices identified with the application of ΔP. $\mathbf{G}^*$ is identified enforcing the equilibrium from (26) and solving the system again in a least-square sense.

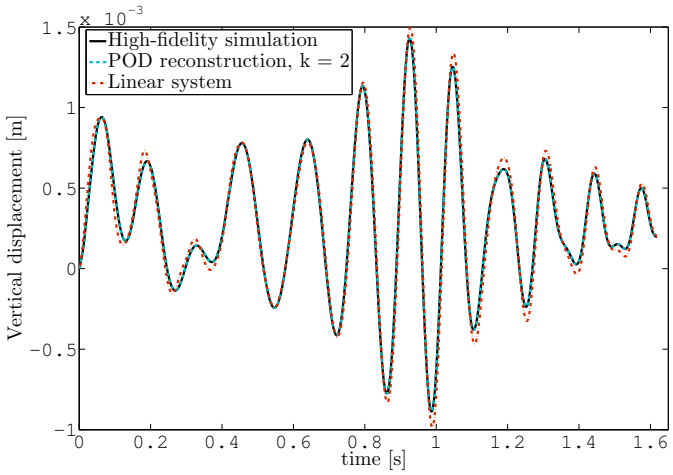


Figure 7: Vertical displacement history of a membrane node with the ΔP harmonic excitation. Comparison of high-fidelity results, POD reconstruction and lower order model results.

The C_l of the membrane is assumed to be a linear function of the states of the system

$$C_l(t) = [\mathbf{C}_{fit}] \begin{bmatrix} \dot{\mathbf{a}}(t) \\ \mathbf{a}(t) \end{bmatrix}, \tag{27}$$

where $[\mathbf{C}_{fit}]$ is the fitting matrix determined solving the system in the least square sense.

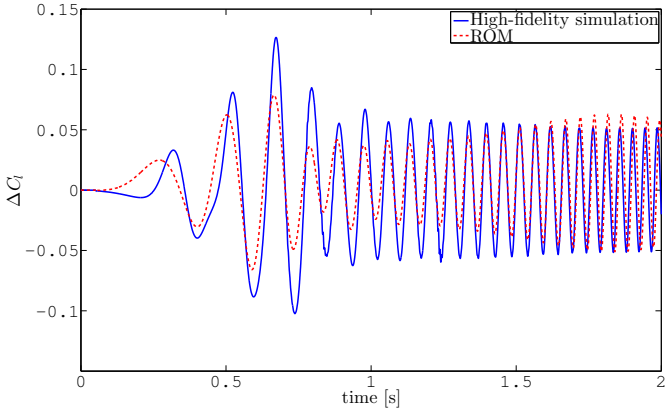


Figure 8: Comparison of the C_l history of high-fidelity and reduced order models for the membrane under harmonic actuation, V = 4.5 kV. The values showed are the absolute variations over the initial reference value, 0.387.

The reduced order model obtained from (26) is used to reproduce high-fidelity simulations of the harmonic actuation of the membrane. The C_l from the harmonic excitation used for the system identification is compared with the results from the low order model in Fig. 8. It can be seen that the very low order description provides a good estimate of the response, which will facilitate the design of the control system in the next section. There are some differences at the very low frequencies and at the resonance peak which are due to the excitation signal used in the system identification. A priori, the system behaviour was not known and a simple linear variation of the signal frequency was chosen. The very low resonance peak requires, instead, a slower frequency evolution. The discrepancy that is observed at the higher frequencies is due to the reduced order of modes considered. However, for the purpose of control system design, the reduced-order model is can be considered as a good estimation of the system dynamic performance.

V.E. Control system design

This reduced-order model is finally used to design a PID-type control system for the wing. The aim is to obtain a given value of the lift coefficient by actuation, starting from a reference passive condition. The low order model allows the definition of the controller gains without the need of multiple runs of the high-fidelity model. The system parameter monitored is the C_l and the input variable of the system is V^2, which is proportional to the Maxwell stress and therefore to the effect of the actuation on the membrane. It needs to be considered that the Maxwell stress is always positive, so when the predicted voltage by the control system is negative, its value is set to zero.The actuation voltage is defined as

$$V^2 = K_p e(t) + K_i \int_0^t e(\tau) d\tau + K_d \frac{d}{dt} e(t) \tag{28}$$

where K_p, K_i and K_d are the proportional, integral and derivative gains respectively, and $e(t) = C_{l,ref} - C_l(t)$ is the instantaneous error between the reference lift coefficient for the control system, $C_{l,ref}$ and the lift coefficient of the system, C_l. The relation in (28) is used also for values of C_l higher than $C_{l,ref}$ together with a lower saturation value set to zero. The initial tuning of the gains of the control system is done with the Ziegler-Nichols method tracking a step $C_{l,ref}$, and relaxing the condition on the lower saturation to zero. The resulting parameters are $K_i = 5.04 \times 10^9$ V/s and $K_p = 1.26 \times 10^8$ V and $K_d = 7.88 \times 10^5$ V. The controller designed is then implemented in the reduced-order model (together with the non-negative condition on the Maxwell stress) to assess its performance and evaluate the effect of the variation of the coefficients (Fig. 9). Numerical results show that, an increase in the proportional and derivative gains destabilise the system and defines large amplitude oscillations of the lift coefficients. Increasing the integral gain results in a faster system response but in an increase in the oscillations as well. Particular care has to be adopted in the design of this kind of control system to avoid the controller to reach the saturation value. The actuation strategy consider, based on the use of Maxwell stresses to relax the membrane tension, does not allow the opposite effect, that is the stiffening of the membrane from the passive condition. In this context, the implementation of a proportional-integral-derivative controller as such can be highly inefficient if fast responses are to be considered, because of the impossibility of acting in both ways.

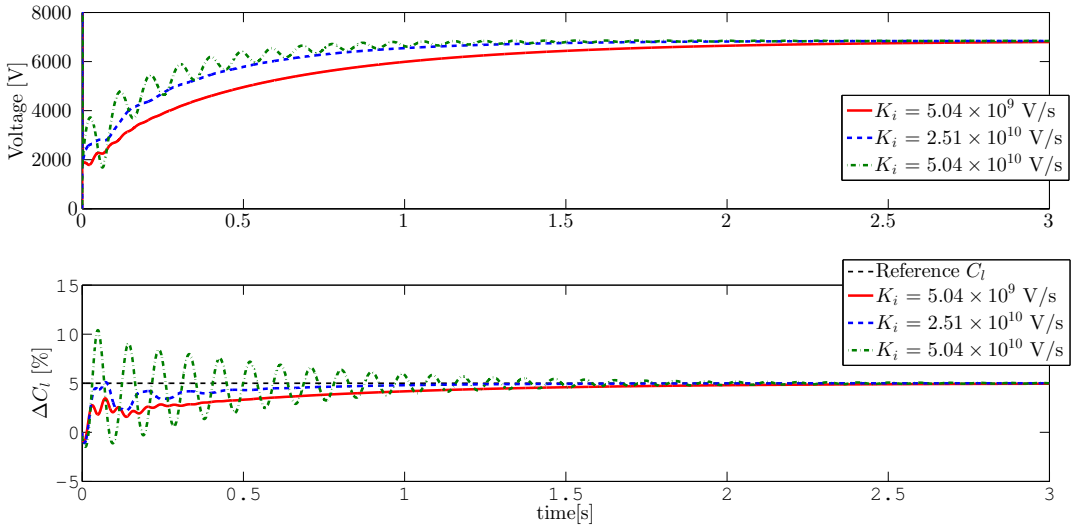


Figure 9: Comparison of the performance of the control system designed in the reduced-order model.

VI. Conclusions

This work has proposed a high-fidelity computational framework for the performance evaluation of actuated membrane wings. The constitutive material model has demonstrated to be predictive of the performance of actuated inflated membranes. The fluid model is based on the direct numerical integration of the

Navier-Stokes equations and its coupling with the structural solver has been verified against results from the literature. The integral actuation of the 2D wing showed that for the cases considered an increase of 6% of the aerodynamic performance of the wing can be obtained, although further investigation of the total energy balance and different flow conditions needs to be considered. Finally a methodology was introduced for the reduced order modelling and control design of the membrane actuation based on proper orthogonal decomposition. The high-fidelity system was excited with input signals to characterise the dynamics of the actuated wing in the frequency range of interest, and the POD projection allowed the definition of a very low order model that can capture the main features of the system. The linear system identified was used to tune the coefficients of a simple control system to track a reference requirement in the aerodynamic performance, a step increase in the C_l. Numerical results need to be compared with the performance prediction from the implementation of the control system in the high-fidelity model.

Acknowledgements

The authors would like to thank Sonia Tiomkin from the Technion for her help with the validation of the model. They also acknowledge the financial support of the European Office of Aerospace Research & Development of the US Air Force Office of Scientific Research, and the UK Engineering and Physical Sciences Research Council Grant EP/J002070/1, "Towards Biologically-Inspired Active-Compliant-Wing Micro-Air-Vehicles".

Appendix

Consider an infinitesimal membrane element laying on the xy plane of length δs and projection on the x axis δx, uniform thickness h and density ρ. The element is subjected to the internal in-plane stresses σ_x and external uniform pressure difference across the membrane ΔP in the y direction. Considering Newton's second law in the vertical direction, we have[15]

$$\frac{\partial^2 y}{\partial x^2} = -\frac{\Delta P}{T_x} \tag{29}$$

where $T_x = \sigma_x h$. When shear stresses are applied to the membrane, an additional equilibrium equation needs to be considered

$$\frac{\partial T_x}{\partial x} = -\tau_x \tag{30}$$

where τ_x is the total shear stress on the membrane element, given by the sum of the shear stresses on the two surfaces. In the general case the stresses depend on the deformation, so the effective tension needs to be updated with the membrane deformation, but in this case the membrane is assumed to be inextensible.

If an inextensible membrane subjected to a uniform difference of pressure distribution, the deformed shape is parabolic. If the membrane extremes are $x(0) = 0$ and $x(c) = 0$ where c is the chord length, the deformed geometry is

$$y = -\frac{\Delta P}{2T_x} x\,(x - c) \tag{31}$$

The maximum height of the camber is found for $x = \frac{c}{2}$ and it is $\frac{y_{max}}{c} = \frac{1}{8\Pi}$ where $\Pi = \frac{T}{\Delta P c}$ is a non-dimensional parameter[13] relating the membrane stiffness to the loading conditions. Song *et al.*[50] found that the mean pressure distribution on a parabolically-shaped inextensible membrane in a fluid flow can be approximated by

$$\Delta P_{mean} = \frac{1}{2}\rho V_\infty^2 C_l c \tag{32}$$

where ρ is the fluid density, V_∞ is the modulus of free stream velocity, C_l is the lift coefficient and c is the chord.

Considering the aforementioned flow assumptions, the lift coefficient of a rigid profile with zero thickness and a parabolic camber is given by[41] $C_l = 2\pi\left(\alpha + \frac{y_{max}}{c}\right)$, where C_l is the lift coefficient, α is the angle of attack of the freestream velocity. Combining the equations and solving for C_l we obtain

$$C_l = 2\pi \frac{1}{1 - \frac{\pi}{4\Pi_\infty}} \alpha \tag{33}$$

where Π_∞ is $\frac{T_x}{\frac{1}{2}\rho V_\infty^2}$.

References

[1]Winter, Y. and Von Helversen, O., "The energy cost of flight: do small bats fly more cheaply than birds?" *Journal of Comparative Physiology B*, Vol. 2, 1998, pp. 105–111.

[2]Newman, B., "Aerodynamic theory for membranes and sails," *Progress in Aerospace Sciences*, Vol. 24, 1987, pp. 1–27.

[3]Rojratsirikul, P., Wang, Z., and Gursul, I., "Unsteady fluid structure interactions of membrane airfolis at low Reynolds numbers," *Experiments in Fluids*, Vol. 46, 2009, pp. 859–872.

[4]Rojratsirikul, P., Wang, Z., and Gursul, I., "Effect of pre-strain and excess length on unsteady fluid-structure interactions of membrane airfoils," *Journal of Fluids and Structures*, Vol. 26, 2010, pp. 259–276.

[5]Rojratsirikul, P., Wang, Z., and Gursul, I., "Flow-induced vibrations of low aspect ratio rectangular membrane wings," *Journal of Fluids and Structures*, Vol. 27, 2011, pp. 1296–1309.

[6]Arbos-Torrent, S., Ganapathisubramani, B., and Palacios, R., "Leadind- and trailing-edge effects on the aeromechanics of membrane aerofolis," *Journal of Fluids and Structures*, Vol. 38, 2013, pp. 107–126.

[7]Bleischwitz, R., de Kat, R., and Ganapathisubramani, B., "Effects of aspect ratio on fluid-structure interactions in membrane wings," *AIAA Scitech, 52nd Aerospace Sciences Meeting, 13-17 January 2014, National Harbor, Maryland*, 2014.

[8]Fox, J. and Goulbourne, N., "On the dynamic electromechanical loading of dielectric elastomer membranes," *Journal of the Mechanics and Physics of Solids*, Vol. 56, 2008, pp. 2669–268.

[9]Fox, J. and Goulbourne, N., "Electric field-induced surface transformations and experimental dynamic characteristics of dielectric elastomer membranes," *Journal of the Mechanics and Physics of Solids*, Vol. 57, 2009, pp. 1417–1435.

[10]Wissler, M. and Mazza, E., "Electromechanical coupling in dielectric elastomer actuators," *Sensors and Actuators A: Physical*, Vol. 138, 2007, pp. 384–393.

[11]Hays, M., Morton, J., Dickinson, B., Uttam, K., and Oates, W., "Aerodynamic control of micro air vehicle wings using electroactive polymers," *Journal of Intelligent Material Systems and Structures*, Vol. 24, pp. 862–878.

[12]Curet, O., Carrere, A., Waldman, R., and Breuer, K., "Aerodynamic characterisation of a wing membrane with variable compliance," *AIAA Journal*, Vol. 52, 2014, pp. 1749–1756.

[13]Smith, R. W. and Shyy, W., "Computational model of flexible membrane wings in steady laminar flow," *AIAA Journal*, Vol. 33, 1995, pp. 1769–1777.

[14]Tiomkin, S., Raveh, D., and Arieli, R., "Parametric study of a two-dimensional membranw wing in viscous laminar flow," *29th AIAA Applied Aerodynamics Conference, 27-30 June 2011, Honolulu, Hawaii*, 2011.

[15]Gordnier, R. E., "High fidelity computational simulation of a membrane wing airfoil," *Journal of Fluids and Structures*, Vol. 25, 2009, pp. 897–917.

[16]Lian, Y., Shyy, W., Viieru, D., and Zhang, B., "Membrane wing aerodynamics for micro air vehicles," *Progress in Aerospace Sciences*, Vol. 39, 2003, pp. 425–465.

[17]Lian, Y. and Shyy, W., "Laminar-Turbulen transition of a low Reynolds numbe rigid or flexible airfoil," *AIAA Journal*, Vol. 45, 2007, pp. 1501–1513.

[18]Visbal, M., "High-fidelity simulation of transiitonal flows past a plunging airfoil," *AIAA Journal*, Vol. 47, 2009, pp. 2685–2697.

[19]Mokarram, H., Vu, D., and Steinmann, P., "Experimental study and numerical modelling of VHB 4910 polymer," *Computational Materials Science*, Vol. 59, 2012, pp. 65–74.

[20]Buoso, S. and Palacios, R., "A nonlinear viscoelastic model for electroactive inflated membranes," *11th World Congress on Computational Mechanics (WCCM XI), Barcelona, 20-25 July*, 2014.

[21]Shian, S., Diebold, R., and D.R.Clarke, "Tunable lenses using transparent dielectric elastomer actuators," *Optical Society of America*, Vol. 21, 2010, pp. 8669–8676.

[22]Raveh, D., "Reduced order models for nonlinear unsteady aerodynamics," *AIAA Journal*, Vol. 39, 2001, pp. 1417–1429.

[23]Feng, Z. and Soulaïmani, A., "Investigation of nonlinear aeroelasticity using a educed order fluid model based on POD method," *18th AIAA Computational Fluid Dynamics Conference, 25-28 June 2007, Miami, FL*, 2007.

[24]Hesse, H. and Palacios, R., "Reduced-order aeroelastic models for dynamics of a maneuvering flexible aircraft," *AIAA Journal*, Vol. 52, 2014, pp. 1717–1732.

[25]Rowley, C., "Model reduction for fluids, using balanced propert orthogonal decomposition," *International Journal of Bifurcation and Chaos*, Vol. 15, 2005, pp. 997–1013.

[26]Kerschen, G., Golinval, J., Vakakis, A., and Bergman, L., "The method of proper orthogonal decomposition for dynamical characterisation and order reduction of mechanical systems: an overview," *Nonlinear Dynamics*, Vol. 41, 2005, pp. 147–169.

[27]Attar, P. and Dowell, E., "A reduced order system ID approach to the modelling of nonlinear structural behaviour in aeroelasticity," *Journal of Fluids and Structures*, Vol. 21, 2005, pp. 531–542.

[28]Lieu, T., Farhat, C., and M.Lesoinne, "Reduced-order fluid/structure modelling of a complete aircraft configuration," *Computer methods in applied mechanics and engineering*, Vol. 195, 2006, pp. 5730–5742.

[29]Liberge, E. and Hamdouni, A., "Reduced order modelling via proper orthogonal decomposition (POD) for flow around an oscillating cylinder," *Journal of Fluids and Structures*, Vol. 26, 2010, pp. 292–311.

[30]Zhang, B., Lian, Y., and Shyy, W., "Propert orthogonal decomposition for three-dimensional membranw wings aerodynamics," *33rd AIAA Fluid Dynamics Conference and Exhibit, 23-26 June 2003, Orlando, Florida*, 2003.

[31]Khalil, M., Adhikari, S., and Sarkar, A., "Linear system identification using proper orthogonal decomposition," *Mechanical Systems and Signal Processing*, Vol. 21, 2007, pp. 3123–3145.

[32]Dassault System, *SIMULIA ABAQUS FEA 6.13, User Documentation*, 2013.

[33]Bonet, J., "Large strain viscoelastic constitutive models," *International Journal of Solids and Structures*, Vol. 38, 2001.

[34]Bonet, J. and Wood., R., *Nonlinear continuum mechanics for finite element analysis*, Cambridge, UK: Cambridge University Press, 2008.

[35]Simo, J. and Hughes, T., *Computational inelasticity*, Springer: Interdisciplinary applied mathematics: Mechanics and materials, 1998.

[36]Flory, P., "Thermodynamic relations for high elastic materials," *Transactions of the Faraday Society*, Vol. 57, 1961, pp. 829–838.

[37]Schmidt, A., Bergamini, A., Kovacs, G., and Mazza, E., "Multiaxial mechanical characterization of interpenetrating polymer network reinforced acrylic elastomer," *Experimental Mechanics*, Vol. 51, 2011, pp. 1421–1433.

[38]Gent, A., "A new constitutive relation for rubber," *Rubber Chemistry Technology*, Vol. 69, 1996.

[39]Suo, Z., "Theory of dielectric elastomers," *Acta Mechanica Solida Sinica*, Vol. 23, 2010, pp. 549–577.

[40]Suchocki, C., "A finite element implementation of Knowles stored-energy function: theory, coding and applications," *The Archive of mechanical engineering*, Vol. LVIII, 2011, pp. 319–346.

[41]Katz, J. and Plotkin, A., *Low-speed aerodynamics*, Cambridge aerospace series, Cambridge University Press, New York, 2nd ed., 2008.

[42]Murua, J., Palacios, R., and Graham, J., "Applications of the unsteady vortex-lattice method in aircraft aeroelasticity and flight dynamics," *Progress in Aerospace Sciences*, Vol. 55, 2012, pp. 46–72.

[43]CD-adapco, *User guide, STAR-CCM+ version 8.04*, 2013.

[44]Pope, S., *Turbulent flows*, Cambridge University Press, New York, 1st ed., 2000.

[45]Valen-Sendstad, K., Mardal, K., Mortensen, M., Reif, B., and Langtangen, H., "Direct numerical simulation of transitional flow in a patient-specific intercranial aneurysm," *Journal of Biomechanics*, Vol. 44, 2011, pp. 2826–2832.

[46]Karhunen, K., "Zur Spektraltheorie Stochasticher Prozesse," *Annales AcademiæScientiarum FennicæSeries A*, Vol. 37, 1946, pp. 3–76.

[47]Loeve, M., *Probability theory*, Van Nostrand, Princeton, 1955.

[48]Lumley, J., "The structure of inhomogeneous turbulence," *A. Yalgom, V. Tatarski (Eds.), Atmospheric turbulence and wave propagations*, Nauka, Moscow, 1967, pp. 166–178.

[49]Buljak, V., *Inverse Analyses with Model Reduction*, Computational FLuid and Solid Mechanics, Springer, 2011.

[50]Song, A., Tian, X., Israeli, E., Galvao, R., Bishop, K., Swartz, S., and Breuer, K., "Aeromechanics of membrane wings with implications for animal flight," *AIAA Journal*, Vol. 46, No. 8, 2008, pp. 2096–2106.

[51]Molki, M. and Breuer, K., "Oscillatory motions of a prestrained compliant membrane caused by fluid-membrane interaction," *Journal of Fluids and Structures*, Vol. 26, 2010, pp. 339–358.